Damage accumulation analysis of cfrp cross-ply laminates under different tensile loading rates

Li, X.; Saeedifar, M.; Benedictus, R.; Zarouchas, D.

DOI
10.1016/j.jcomc.2020.100005

Publication date
2021

Document Version
Final published version

Published in
Composites Part C

Composites Part C: Open Access 1 (2020) 100005

Contents lists available at ScienceDirect

Composites Part C: Open Access

journal homepage: www.elsevier.com/locate/jcomc

Damage accumulation analysis of cfrp cross-ply laminates under different tensile loading rates

Xi Li, Milad Saeedifar, Rinze Benedictus, Dimitrios Zarouchas*

Structural Integrity & Composites Group, Faculty of Aerospace Engineering, Delft University of Technology, Kluyverweg 1, 2629HS, The Netherlands

ARTICLE INFO

Keywords:
Transverse matrix crack
Inter-laminar crack
Acoustic emission
Digital image correlation
Cross-ply laminate

ABSTRACT

This paper investigates the loading rate effect on both mechanical properties and damage accumulation process of $[0^{\circ}_2/90^{\circ}_4]_S$ carbon fiber-polymer laminates under tensile loading. In-situ edge observations, Acoustic Emission and Digital Image Correlation techniques were utilized simultaneously to monitor the state of damage in real time. Results showed that the axial modulus and strength were less sensitive to loading rates than failure strain, which increased with the decrease of the loading rate. In the viewpoint of damage accumulation process, high density and uniform distribution of transverse matrix cracks, and H-shape crack patterns, incorporating inter-laminar cracks, were more likely to occur at low loading rates while variable crack spacing occurred at higher rates. When loading rates were lower than a certain level, maximum transverse matrix crack density decreased slightly due to the restriction of relatively widely generated inter-laminar cracks. Furthermore, the cumulative acoustic emission energy of low-frequency signals was linearly correlated to transverse matrix crack density, providing a promising way to quantify crack accumulation in real time. Finally, spatial consistence was observed between transverse matrix cracks at edges and stress concentrations at the exterior 0° ply, and the peaks of axial strain at local concentration regions locate either near the newest cracks or at the place with minimum crack spacing.

1. Introduction

Composite structures may experience loading combinations which vary from static loads induced by its own weight to high-strain-rate loads like impact. Considering the uncertain service environment, it is important to explore and understand the loading rate effects on the mechanical response and damage accumulation process.

A plethora of studies exist for different types of polymer materials that deal with the mechanical response under different loading rates, mainly carbon and glass fiber reinforced polymers (CFRP and GFRP), and lay-up configurations, such as unidirectional (UD) laminates [1–3], multi-directional laminates [2,4,5], woven composites [3]. These studies show that CFRPs are generally less sensitive to loading rates in comparison with GFRPs [4,5]. Zhang et al. [3] found that loading-rate-dependency of the tensile strength, Young's modulus and failure strain of UD CFRP laminate, was not obvious under 20 s^{-1} while a remarkable increase was observed at the rate over 20 s^{-1}. Taniguchi et al. [1] reported that the tensile modulus and strength were independent of loading rates for $[0^{\circ}]$ laminates, but an increase of the tensile modulus and strength with the increase of loading rates was observed for $[90^{\circ}]$ and $[45^{\circ}]$ specimens. Gilat et al. [2] concluded that the loading-rate-effect on the maximum stress of $[45^{\circ}]$ and $[\pm45^{\circ}]_S$ specimens was more significant than of $[90^{\circ}]$ and $[10^{\circ}]$ specimens.

The fact that off-axis laminates are sensitive to loading rates implies that their damage accumulation process, especially for matrix-related damage mechanisms, is different for different loading rates. Few studies [6–8] dealt with the loading rate effects on the evolution of transverse matrix cracks, and Berthe and Ragonet [8] concluded that the rate sensitivity is stronger for low strain rates than for intermediate strain rates. Azadi et al. [9] found that the loading rate did not alter the dominant damage mechanism, but the quantity of each damage mechanism changed with different loading rates, an observation that the authors believe needs further research.

For the non-transparent CFRP composites, the main challenge is to quantitatively identify matrix-related damage mechanisms in real time [10]. As the most direct way, optical edge observation by cameras or microscopes is capable to track the crack accumulation for the rectangular laminated coupons with off-axis plies [11–14]. However, in view that high resolution and large observation window are usually hard to be achieved simultaneously, in-situ crack characterization in the large-size view window remains challenges for non-interrupted tests. In most cases, specimens need to be removed from the testing machines, or tests need to be interrupted for ex-situ/in-situ damage inspections, which can induce the stress relaxation and further affect the cracking process [10]. Cho et al. [15] found that both the crack density and maximum stress during the loading and unloading phase of tensile tests were strongly

* Corresponding author.
E-mail address: d.zarouchas@tudelft.nl (D. Zarouchas).

https://doi.org/10.1016/j.jcomc.2020.100005
Received 22 April 2020; Received in revised form 13 July 2020; Accepted 15 July 2020

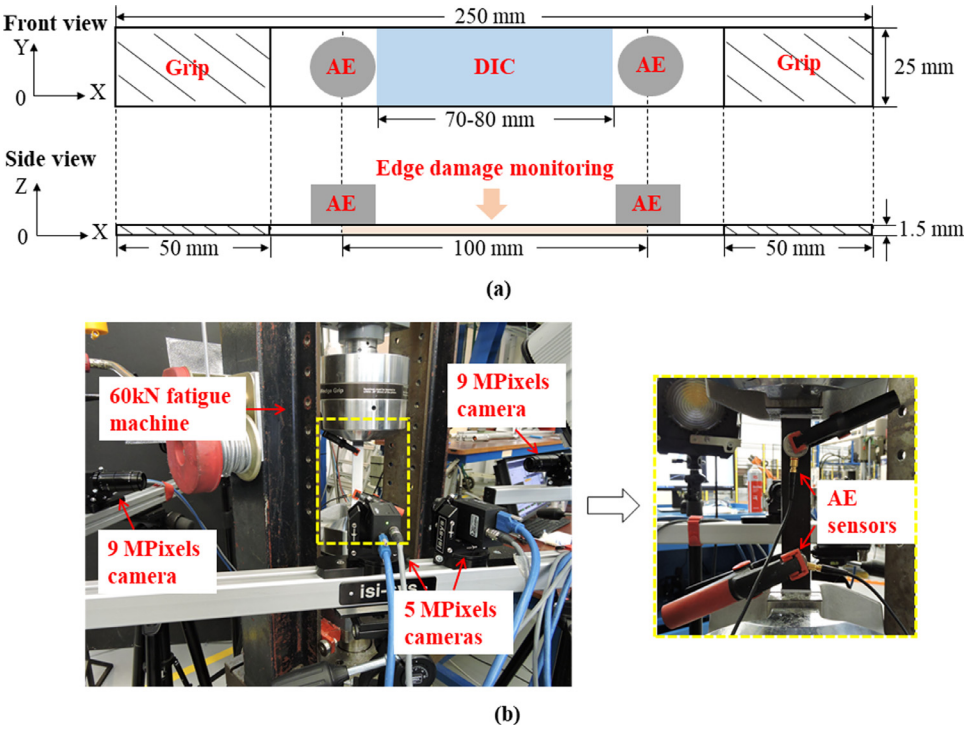

Fig. 1. The schematic diagram of specimen dimensions, AE sensors' locations, measurement area of DIC and clamping regions (a); Experimental equipment (b).

dependent on the particular loading sequence, and a time-dependent increase in matrix cracks occurred throughout the hold period.

Advanced in-situ monitoring techniques like Digital Image Correlation (DIC) [10–12,16,17], infrared thermography (IR) [8,18,19] and Acoustic Emission (AE) [9,11–13,19–22] have also been widely applied for CFRP composites to help detect different failure mechanisms and monitor the damage accumulation process.

By applying DIC, Tessema et al. [16] investigated the matrix crack initiation and gradual propagation of quasi-isotropic laminates using the local concentration of axial and shear strain as damage indicators of intra-laminar and inter-laminar cracks. Mehdikhani et al. [10] quantified the evolution of transverse matrix cracks of cross-ply laminates by counting the peaks of the strain profile via both macro- and meso- scale DIC analysis. However, detecting the damage accumulation in this way is highly affected by the ply thickness and the stacking sequence of laminates [11].

As for IR, the variation of surface temperature can represent the degradation and dissipative mechanisms of material [18], but different damage mechanisms are hard to be precisely characterized and localized according to the heat sources, especially for matrix cracks which dissipates less thermal energy than fiber damage and interface failure [19]. Recently, Berthe and Ragonet [8] have achieved the monitoring of matrix cracking appearance by using passive infrared thermography measurements for cross-ply laminates with 41 mm free length between tabs.

Compared with DIC and IR, AE provides more informative damage-related results and it is regarded as the most promising technique to uncover the initiation and progression of different damage mechanisms [11]. Intensive efforts have been made on the interpretations of AE activities by analysing multiple AE features with clustering algorithms involved. A recent review on the damage analysis of composite structures using AE highlights the potential of this monitoring technique [25]. Amplitude and frequency are treated as the most preferred AE features to classify different AE activities [11,19,20,22–24]. To correlate AE clusters to different damage mechanisms, some researchers have executed destructive tests on the individual constituent materials, for example coupons made of pure resin or fiber bundles, to obtain the AE feature of each damage mechanism separately. These AE features were then used as the reference patterns to correlate each AE cluster to a specific damage mechanism [9,22–24]. A general trend has been established which relates AE waveforms with low peak frequency and amplitude to matrix-cracking-related damage mechanisms [22–24]. However, doubts exist in view that AE features for each damage mechanism might be different for composite samples with different dimensions [21] or stacking sequences [11].

Therefore, it is necessary to combine AE and other monitoring systems during the tests to provide a reliable interpretation of AE activities and corresponding features. Oz et al. [11,12] correlated AE clusters obtained from k-means++ algorithm to different damage mechanisms (*e.g.* matrix cracks at the surface and inner 90° plies, micro and macro delamination, *etc.*) monitored from optical edge observation and DIC. They found that the depth of damage source can affect the corresponding AE features and high frequency could also be induced by the matrix cracking when 90° plies approach to mid-section of specimens. Baker et al. [13] concluded that waveform-based AE energy can be used to identify matrix crack initiation observed by the optical microscope from the edge. These observations indicate AE activities could be comprehensively interpreted to identify different damage mechanisms, and the evolution of AE features from different clusters are expected to act as the indicators to quantitatively represent the accumulation of different damage mechanisms in the future.

The objectives of present work were to investigate the loading-rate-dependency of both mechanical properties and damage accumulation process for CFRP cross-ply laminates under tensile loading, and to explore the correlations of damage-related results from different in-situ monitoring systems. In the test campaign, thick 90° block in the middle of cross-ply laminates were designed to provide detectable cracks, and optical edge observation, DIC and AE were applied simultaneously to monitor the crack accumulation process. The main contribution of present work is the achievement of in-situ characterization of transverse

Table 1
The control mode, loading rate, running time and strain rate under each load condition.

Control mode	Loading rate	Running time (s)	Strain rate (s^{-1})
Load	0.019 kN/s	1470.25 ± 40.14	9.77×10^{-6}
	0.19 kN/s	140.72 ± 1.78	9.98×10^{-5}
	1.9 kN/s	14.21 ± 0.03	9.56×10^{-4}
	19 kN/s	1.54 ± 0.01	8.52×10^{-3}
Displacement	1 mm/min	196.80 ± 3.05	7.19×10^{-5}

Table 2
Mechanical properties of cross-ply laminates under different loading rates.

Loading rate	Axial modulus (GPa)	Tensile strength (MPa)	Failure strain
0.019 kN/s	51.45 ± 0.65	706.81 ± 14.91	0.0144 ± 0.0002
0.19 kN/s	50.54 ± 0.70	684.99 ± 7.82	0.0140 ± 0.0002
1.9 kN/s	51.26 ± 1.01	691.01 ± 15.69	0.0136 ± 0.0001
19 kN/s	51.32 ± 2.18	± 8.34	0.0131 ± 0.0000
1 mm/min	± 0.32	699.33 ± 6.94	0.0141 ± 0.0002

matrix cracks and inter-laminar cracks in a large view window (100 mm) without interrupting the tensile tests, which further enriches the analysis of loading-rate-effect on the statistical distribution of transverse matrix cracks and enhances our understanding on how inter-laminar cracks constrain the generation of transverse matrix cracks.

2. Experimental methods

2.1. Material and specimens

The specimens used in the present study were manufactured from the UD carbon fiber Prepreg named Hexply® F6376C–HTS(12 K)–5–35%. This Prepreg system contains high tenacity carbon fibres (Tenax®-E-HTS45) and high-performance tough epoxy matrix (Hexply® 6376). The nominal fiber weight ratio and thickness of the Pregreg are 65% and 0.125 mm, respectively. The material properties of the UD-Prepreg layer in cured condition can be found in [26].

Two 600 × 300 mm^2 panels were laminated following the stacking sequences of $[0^\circ_2/90^\circ_4]_S$. They were then cured inside an autoclave according to the manufacturer's recommendation [27]. Afterwards, the panels were cut, using a water-cooling diamond saw, into rectangular specimens of 250 mm × 25 mm according to ASTM D3039/D3039M-17 standard [28], as shown in Fig. 1(a).

Thick paper tabs were glued on both ends of the specimen using cyanoacrylate adhesive in order to increase clamping grip. Additionally, both edges of the specimen were covered with thin white paint to enhance the quality for the damage monitoring with the edge cameras. Finally, a white base coat was painted on the front surface of specimen and then designed speckle pattern with the dot size of 0.18 mm were printed on the surface using a VIC speckle roller to prepare the DIC inspection area.

2.2. Test set-up

2.2.1. Tensile test

Tensile tests were carried out on a 60 kN fatigue machine with hydraulic grips, as shown in Fig. 1(b). Five levels of loading rates were performed under load and displacement control mode, as listed in Table 1. The corresponding running time and strain rate at each rate are also presented in Table 1. Here, the strain rate equals to the strain at peak loads divided by the running time. The 1 mm/min and 0.19 kN/s can be regarded as similar loading rates based on the strain-rate level.

To guarantee the repeatability of test results, five specimens were tested under each loading rate while specimens that fail at the clamps were excluded from the analysis. The AE, DIC and edge damage monitoring systems were synchronized with the testing machine to create a synergistic work environment among different devices.

2.2.2. Edge damage monitoring system

Two 9 Megapixel cameras with 50 mm lens and 150 frames-per-second were placed at left and right side of the testing machine to monitor cracks occurred on both edges of the specimen, as shown in Fig. 1(b). A total length of 100 mm for each edge was observed during the test. After testing, the number and position of cracks at the 90° plies were obtained through a user-defined MATLAB code. Initially, the acquired images were processed using a Bottom-hat filtering in order to compute the morphological closing of the image. Then, the filtered images were subtracted from the original ones allowing the contrast of crack and un-cracked regions at the edges to be enhanced. Finally, the processed images were converted to binary images in order to label the cracks as regions of contiguous white pixels, for being later counted and localized.

2.2.3. AE system

Two broadband VS900-M AE sensors with a diameter of 20.3 mm and a frequency range of 100–900 kHz were clamped on the specimen. The distance between two sensors was fixed to 100 mm for all tests, as shown in Fig. 1(a). Vacuumed silicon grease was used between the AE sensor and the specimen surface to create good acoustical coupling. The AMSY-6 8-channel Vallen system was used to record the AE activity and two pre-amplifiers with gain of 34 dB and band-pass filter of 20–1200 kHz were used to connect the sensors to the AE system. Before each test, pencil lead breaks were performed to calibrate the data acquisition system. In all tests, the sampling rate and threshold were set as 2 MHz and 45 dB, respectively.

2.2.4. DIC system

The DIC was employed to measure the displacement and strain distributions of the exterior 0° ply. In the present study, two different positions of a specimen can be applied with DIC system to monitor the strain/displacement distributions during the test, *i.e.* the edge and the exterior 0° ply. Considering the thickness of the specimens (~1.5 mm), it is extremely difficult to monitor the entire edge with accurate measurements. Furthermore, the speckle pattern, applied on the edges, could affect the contrast of edge images and disturb the identification of transverse matrix cracks during the post image processing. Therefore, a pair of 5 Megapixel cameras with 23 mm lens and 75 frames-per-second was

Table 3
Load level and location when the transverse matrix crack initiated at different loading rates.

Loading rate	Load level F/F_{max} (%)			Location X (mm)		
	Specimen #1	Specimen #2	Specimen #3	Specimen #1	Specimen #2	Specimen #3
0.019 kN/s	81.88	61.32	85.66	79.49	29.15	88.95
0.19 kN/s	82.43	52.50	66.07	35.42	71.59	24.75
1.9 kN/s	83.24	85.00	78.79	91.33	66.26	38.67
19 kN/s	73.02	75.01	87.12	67.94	44.50	18.77
1 mm/min	76.30	69.51	81.00	61.13	73.07	16.05

Note: $X = 0$ mm is at the fixed side of the specimen while $X = 100$ mm is near the loading side.

Table 4
Matrix crack density and crack spacing at the 90° plies under different loading rates.

Loading rate	Maximum matrix crack density ρ_{max} (mm^{-1})	Crack spacing d (mm)			
		$d_{average}$	d_{min}	d_{max}	d_{max}-d_{min}
0.019 kN/s	0.24 ± 0.02	3.64 ± 0.15	1.12 ± 0.75	9.07 ± 1.05	7.95 ± 0.30
0.19 kN/s	0.30 ± 0.04	3.33 ± 0.47	0.57 ± 0.26	10.03 ± 3.59	9.46 ± 3.63
1.9 kN/s	0.16 ± 0.01	5.59 ± 0.32	0.63 ± 0.19	16.43 ± 6.03	15.80 ± 6.12
19 kN/s	0.14 ± 0.02	5.84 ± 0.47	0.44 ± 0.06	19.57 ± 7.71	19.13 ± 7.65
1 mm/min	0.25 ± 0.02	3.84 ± 0.37	0.91 ± 0.67	14.24 ± 3.89	13.33 ± 4.56

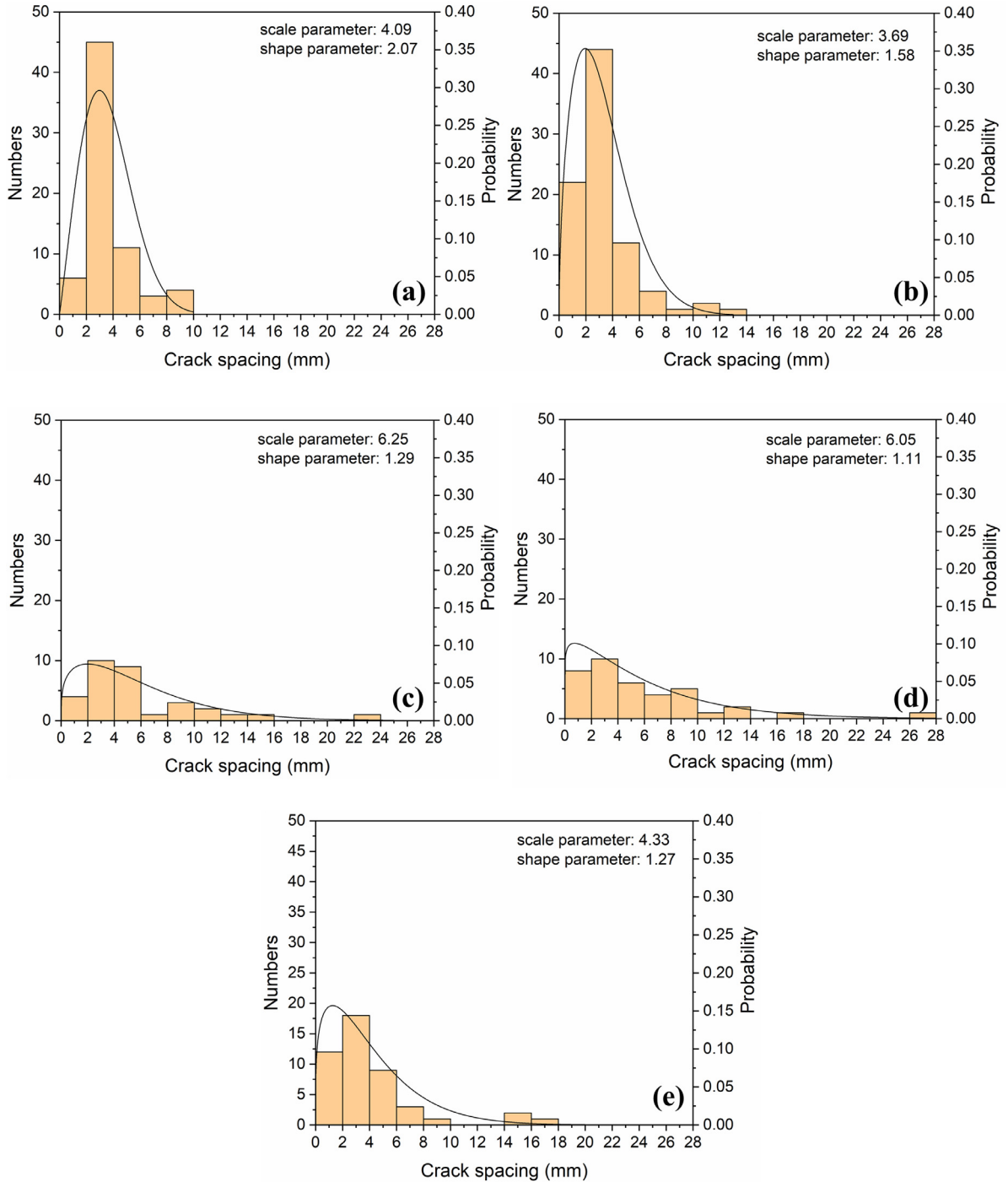

Fig. 2. Histogram of crack spacing between adjacent transverse matrix cracks and related two-parameter Weibull distributions at different loading rates: (a) 0.019 kN/s, (b) 0.19 kN/s, (c) 1.9 kN/s, (d) 19 kN/s, (e) 1 mm/min.

placed in the front side of the specimen, as shown in Fig. 1(b), to measure the global axial deformation and the strain distributions close to the cracked regions of 90° plies. Post-processing was performed using the commercial software VIC-3D by *Correlated Solutions*. A subset size of 29 pixels and step size of 7 pixels were selected for correlation analysis. The length of the view field for in-situ strain measurement was approximately 70–80 mm.

3. Results and discussion

3.1. Mechanical properties

The elastic modulus, tensile strength and failure strain of the specimens under different loading rates are listed in Table 2. The modulus was calculated based on data gathered within the axial strain range less than 0.5%. Failure strain corresponds to the global strain of specimens at the maximum load. The global strain was obtained by tracking the displacement of two points near the top and bottom of the DIC measurement region. An increase can be observed for the failure strain when the loading rate is reduced, which is consistent with the results reported by Gilat et al. [2]. This fact indicates that specimens behaved in a more ductile way at lower loading rates [29]. As the matrix is loading-rate-dependent, its ductile response, such as the stress relaxation and plastic deformation, can be more easily triggered at low loading rates [30,31]. On the other hand, the axial modulus and tensile strength fluctuated at a relatively narrow band and they were less loading-rate-dependent compared with the failure strain response due to the loading-rate-insensitive nature of carbon fibres [32]. Therefore, it can be concluded that the matrix dominantly determines the sensitivity of cross-ply laminates to strain rates in the present study [2].

3.2. Damage on the edge

3.2.1. Transverse matrix cracks

Table 3 lists the positions and the load levels when the first matrix crack occurs at the 90° plies for three specimens at each rate. For all specimens, the first matrix crack occurred at an arbitrary position of the inner 90° plies and the corresponding load level is distributed in the range from 52.50% to 87.12%. This fact is attributed to the inherent material defects inside the specimens like micro-cracks and voids, which highly affect the origins of the transverse matrix crack [33].

The number of cracks at each side was the same at each loading moment, indicating that the transverse matrix cracks rapidly propagated through the entire width direction. Table 4 lists the maximum matrix crack density and the crack spacing for the different loading rates. Here, the maximum matrix crack density ρ_{max} equals to $N/2$ L, where N is the total number of transverse matrix cracks on both edges before specimens failed and L is the length of the edge observation region. The matrix crack density decreased with the increase of loading rates, except for the 1 mm/min and 0.019 kN/s cases where a slight decrease of matrix crack density is observed. Furthermore, crack-spacing related variables are also listed in Table 4. Crack spacing d means the distance between every two adjacent transverse matrix cracks. The average crack spacing $d_{average}$, the maximum crack spacing d_{max} and the differences between the maximum and minimum crack spacing d_{max}-d_{min} were larger at 1 mm/min (7.19×10^{-5} s^{-1}) than those at 0.19 kN/s (9.98×10^{-5} s^{-1}). This indicates that transverse matrix cracks distributed more unevenly under displacement control mode than under load control mode when the strain-rate level is similar. In the load-controlled cases, d_{max} and d_{max}-d_{min} increased with the increase of loading rates, reflecting the more uniform distribution of transverse matrix cracks at lower loading rates.

Nevertheless, the deviations of all crack-spacing variables were significant, which highlights the spatial stochastic processes of transverse matrix crack [34]. Cho et al. [15] attributed this phenomenon to the fact that the location of subsequent cracks is very sensitive to minor local variations in matrix. To represent better the statistical variation in crack spacing, variable material properties, *i.e.* strength and fracture energy, are usually assumed during crack evolution processes [15,35,36]. Fig. 2 presents the histogram of crack spacing between adjacent transverse matrix cracks. A two-parameter Weibull distribution is utilized in to describe the probabilistic distribution of crack spacing. Under lower loading rate, crack spacing is more likely to concentrate between 2 and 4 mm with narrower scatter band, while a more uniform probability distribution is presented under higher loading rate with wider scatter band. This phenomenon further reflects the large scattering in crack spacing at higher loading rate.

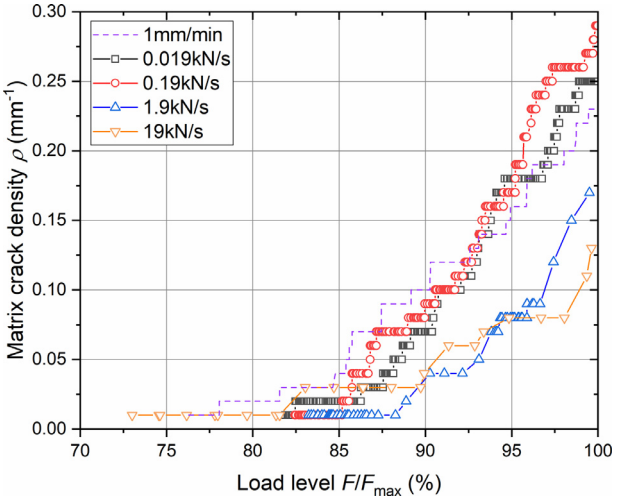

Fig. 3. The growing trend of matrix crack density with the load level.

Fig. 3 presents the matrix crack evolution *versus* the load for every loading rate. The load level F/F_{max} is represented as the percentage of the current load F to the maximum load F_{max}. Under all loading rates, matrix crack density remained constant or presented a slow growing trend up to the load level around 85% and then increased significantly up to the final failure. The higher loading rates (1.9 kN/s and 19 kN/s) exhibited slower increase of matrix crack density than the other three loading rates for which the curves of matrix crack density were similar among each other.

Moreover, the location X and load level F/F_{max} when each transverse matrix crack generated, and the local crack density at every 20 mm edge region are shown in Fig. 4. For a clear visualization, only one representative specimen at each loading rate is selected here. Next to the straight transverse cracks, few curved cracks were observed during the tests, as marked by the black arrows in Fig. 4 and seen in Fig. 5b (specimens 3,4,5 for). Groves et al. [37] reported that the curved cracks are driven by the stress state resulting from the adjacent straight cracks and Hu et al. [38] proposed that they only occur when the crack density of straight cracks exceeds the critical value. In the present work, it was found that they were prone to occur under high load level and locate near one prior straight crack with the spacing less than 1 mm.

Furthermore, the first three transverse cracks were also labelled in Fig. 4 and it assumed that they occurred at the region where the local crack density is relatively high. The new cracks are located around the prior cracks, which is different from what some models propose; that new cracks form midway between existing cracks [39,40]. Moreover, among all local crack regions, a remarkable high crack density was presented where both the curved cracks and one of the first three cracks coexisted. In addition, when the loading rate increased, most transverse matrix cracks initiated at the high load level. For instance, at 19 kN/s, nearly half of total cracks formed just before the final failure.

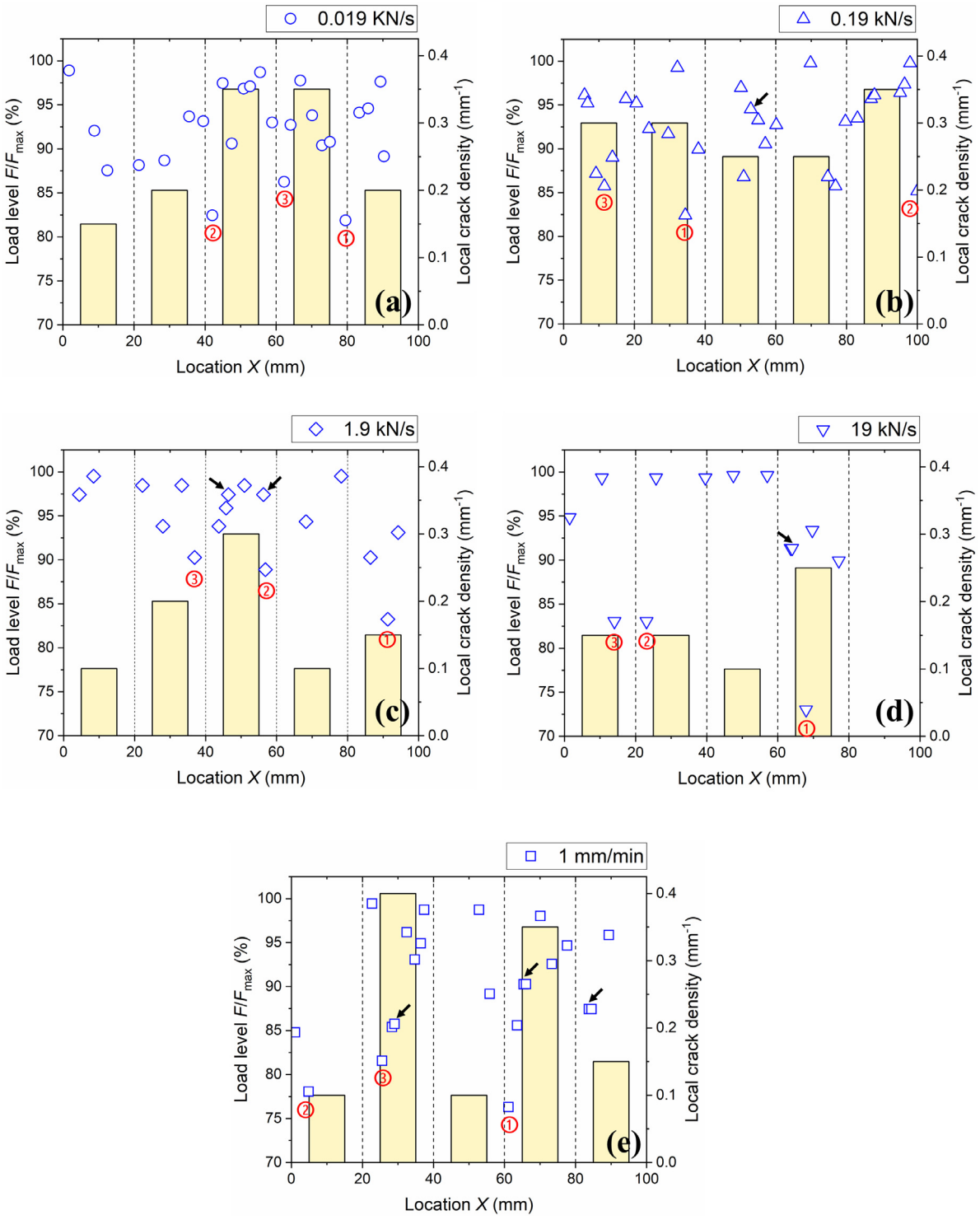

Fig. 4. The location and load level when each transverse matrix crack occurred (scatter plot), and the local crack density at every 20 mm edge region (bat chart) under different loading rates.

3.2.2. *Inter-laminar cracks*

Similar to transverse matrix cracks, inter-laminar cracks located at $0^{\circ}/90^{\circ}$ interfaces were more likely to occur at low loading rates. The inter-laminar cracks promote energy absorption and stress redistribution, but on the other hand they restrict the occurrence of new transverse matrix cracks nearby when inter-laminar cracks are relatively widely distributed along the edge [40].

During the tests, inter-laminar cracks always originated at the tips of transverse matrix cracks. Fig. 5 presents two local regions along the loading direction (*i.e.* $0 \le X \le 25$ mm and $50 \le X \le 75$ mm), where typical morphologies of the co-existing of transverse and inter-laminar cracks at the peak load are highlighted, shaping H, L and T forms. The crack pattern H mainly occurred at the low loading rates. This is because specimens have more time to redistribute the load and absorb energy at low

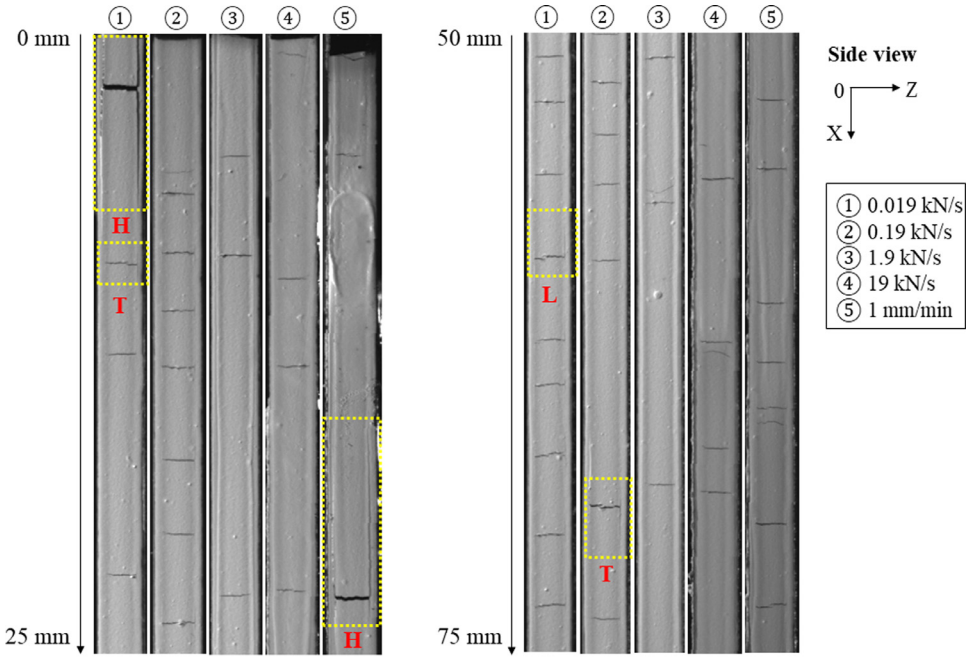

(a) 0 mm ≤ X ≤ 25 mm **(b)** 50 mm ≤ X ≤ 75 mm

Fig. 5. The distribution patterns of co-existing transverse and inter-laminar cracks at two local regions of the specimen edge when reaching the peak load for each loading rate.

rates, and as a result inter-laminar cracks are more probably to occur at both tips of the transverse matrix crack and propagate along both sides of the crack tip.

3.3. AE activity analysis

In the present work, peak frequency was applied as a representative feature to interpret AE activities, because it is less affected by the attenuation happened during the wave propagation in comparison with amplitude, duration, *etc*. [41]. Fig. 6 presents three bands of peak frequency (*i.e.* 100–200 kHz, 300–400 kHz and > 400 kHz) among AE activities at each rate, and the corresponding growing trends of cumulative energy E_{cum} with the increase of the load level. Here, E_{cum} represents the summation of energies of each AE activity, as they are recorded by the data acquisition system - Vallen Systeme [42]. The AE data at 19 kN/s were not further analysed because almost 95% of the number of AE activities occurred at the failure and post failure phases. The formation of distinct frequency bands, as a result of damage accumulation, is determined by material properties, ply configurations and load conditions given the same sensors and acquisition system.

The first AE activity was recorded at around 10% to 30% of the failure load under all the loading rates, while the cumulative energy started to increase at load levels around 60% to 80%. The origin of the early AE activities with negligible cumulative energy indicates the development of micro-cracks before transverse matrix cracks initiated. The highest cumulative energy during the tests was provided by AE activities in the peak frequency range from 100 kHz to 200 kHz, which also presented slower growing trends of cumulative energy in most cases than other AE activities with high frequency.

Among the three groups of AE activities classified by peak frequency, similar growing trends of matrix crack density and cumulative energy as a function of the load level $F/F_{\max}$ were observed for the low frequency band (100–200 kHz), as presented in Fig. 7. Here, both crack density and cumulative energy were normalized by their values at the peak load, as expressed as ρ/ρ_{max} and E_{cum}/E_{cum_max} respectively. Each jump on ρ/ρ_{max} can sufficiently correlate to certain stepping increase of E_{cum}/E_{cum_max}. Therefore, AE activities in the low frequency level were dominantly related to transverse matrix cracks. This conclusion is in coincidence with the majority findings in literature [22–24], but it does not match with what Oz et al. reported [11]. The authors observed that matrix cracks at the inner 90° plies usually generate AE activity with peak-frequency of higher ranges and they explained that the depth of the damage source can affect the AE characteristics. In our study, the thickness of exterior 0° plies is only 0.25 mm, thus the through thickness distance of a matrix crack to AE sensors can barely affect the corresponding AE characteristics.

Furthermore, the normalized matrix crack density ρ/ρ_{max} is plotted against the normalized cumulative AE energy E_{cum}/E_{cum_max} of low-frequency AE activities (*i.e.* 100–200 kHz), where a linear correlation is found, see Fig. 8. This plot demonstrates that the cumulative energy of low-frequency AE activities can describe the accumulation of transverse matrix cracks for cross-ply laminates, which further paves a promising way for the real-time quantification of transverse matrix crack evolution based on AE feature.

3.4. Axial strain distributions

Fig. 9 shows the axial strain distributions at the exterior 0° ply for all tested loading rates under four different loading levels (*i.e.* 85%, 90%, 95% and 100% of the maximum load). For the same load level, it is observed that the local strain at low loading rates was greater than that at high loading rates. When the transverse matrix cracks started to initiate, strain concentrations with narrow strips (2.8 mm to 5.2 mm) occurred through the width of the specimens. As the load increased, some of these strips expanded or connected with their neighbours to form large strain concentrations. At maximum load, the largest strain concentration area at the loading direction, 38 mm, was found for 0.019 kN/s.

To further investigate the development of strain concentrations, the distribution of transverse matrix cracks, obtained from edge observations, was compared with axial strain distributions as measured by DIC. A good correlation of matrix cracks at the inner 90° plies and strain concentrations at the exterior 0° ply under different loading rates is shown in Fig. 10. The red dash boxes at the front surface of specimens were used to label the strain concentration regions with more than one trans-

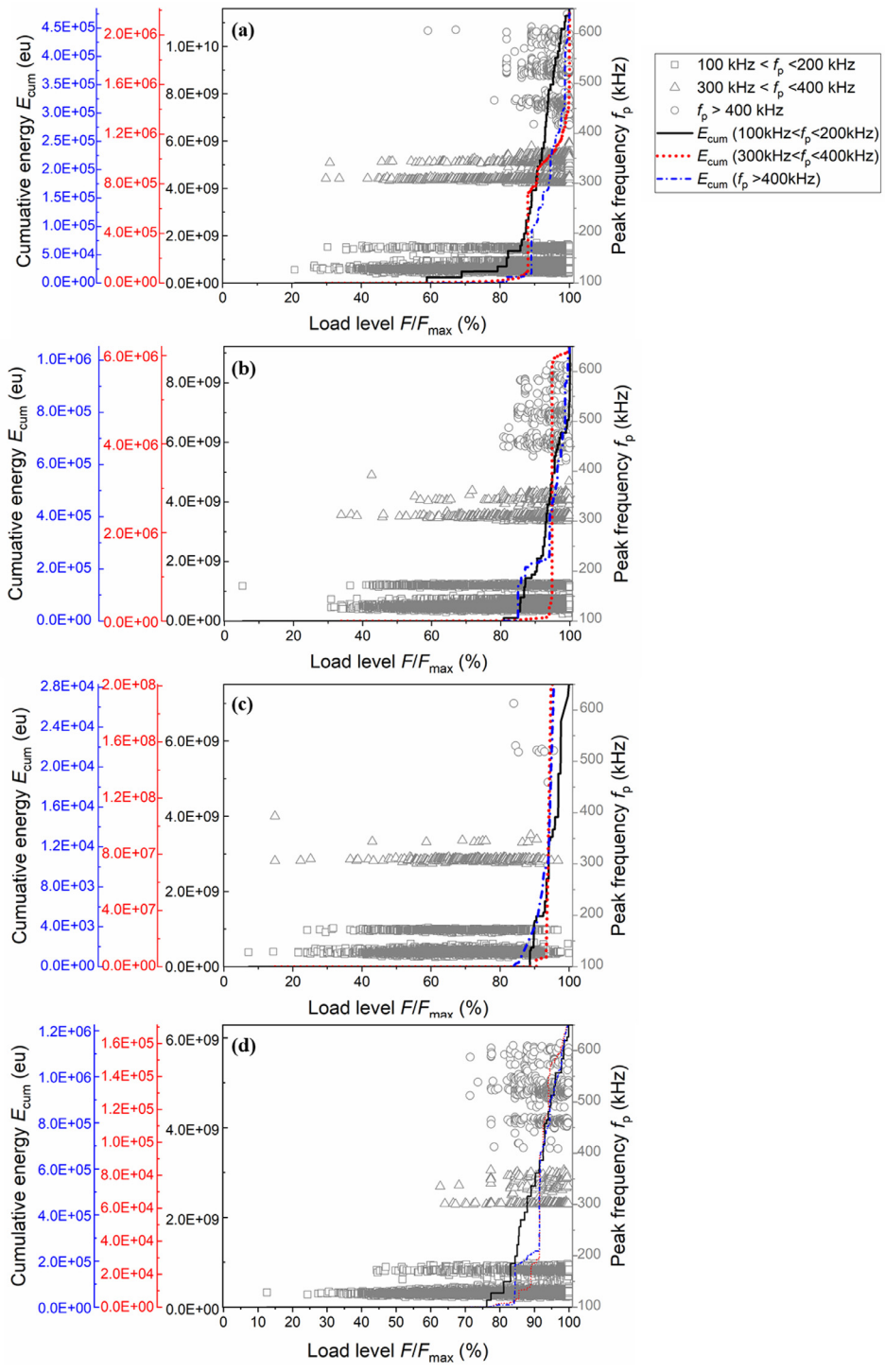

Fig. 6. Three bands of peak frequency among AE activities and the corresponding cumulative energy plotted with the increase of load level under different loading rates: (a) 0.019 kN/s, (b) 0.19 kN/s, (c) 1.9 kN/s, (d)1 mm/min.

verse matrix cracks, generated from the edge thickness and the related transverse matrix cracks at the local region with strain concentration, were marked by the curly brackets at edges. These marked regions were also the places where expansions or connections of strain concentration with narrow strips occurred at each loading rates. As observed, the matrix cracks at 90° plies cause uneven distribution of strain at the 0° plies. In view that the inter-laminar cracks were not widely distributed along the edge and they did not propagate broadly inside the specimens under tensile loading, their effects on the distributions pattern of axial strain are negligible in the present study.

The strain profile of a line slice along the loading direction (as marked with the white solid line in Fig. 10) and related global strain (as plotted with the dash line) at three different moments (*i.e.* t_1, t_2 and t_3) were also presented in Fig. 11. Here, t_1 is the moment that no expansions or connections among individual strain concentrations occur; t_2 is the moment that local strain concentrations start to expand or connect with their neighbours; t_3 is the moment of the maximum load. The first expanding direction of local strain concentrations is marked with red arrow at t_2 and the numbered strain concentration regions at t_3 (red dash boxes at the front surface of specimens) in Fig. 10 were also shown

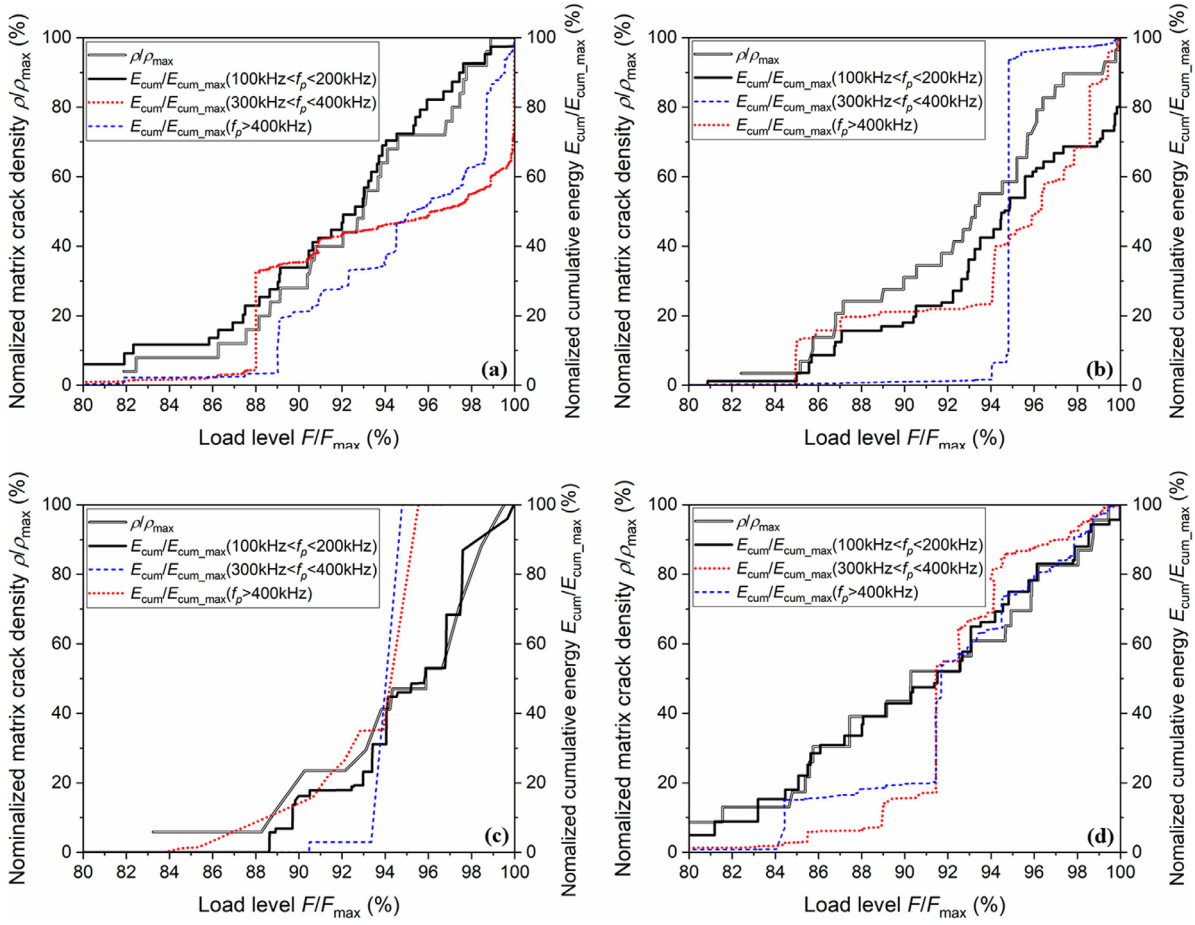

Fig. 7. The normalized matrix crack density and normalized cumulative energy of AE activities located at different frequency bands as a function of the load level under different loading rates: (a) 0.019 kN/s, (b) 0.19 kN/s, (c) 1.9 kN/s, (d)1 mm/min.

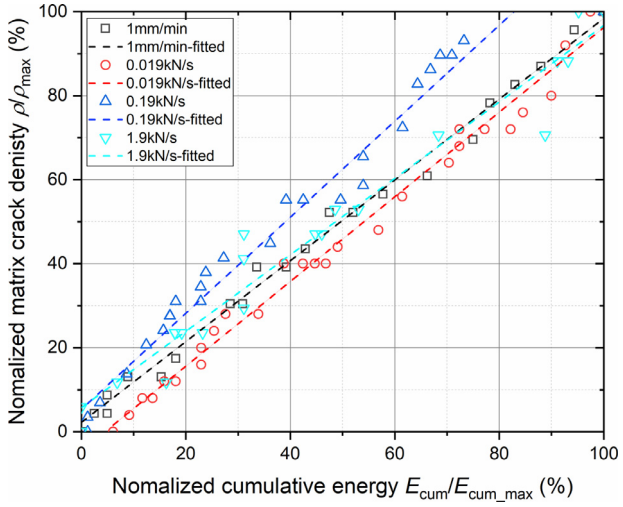

Fig. 8. The relationship between normalized matrix crack density and normalized cumulative energy of low-frequency AE activities at different loading rates.

in the strain profile for each loading rate in Fig. 11. Before t_1, strain concentrations appeared as the narrow strips at the crack location. Afterwards, the new cracks affect the early-emerged strain concentrations, and this is determined by the distance between the new cracks and their neighbours. If the crack spacing is small enough, less than 4 mm, the original strain concentration expands to cover the region with the high local crack density. Otherwise, only new strain concentration strips are induced. This further explains why the largest strain concentration region was generated at the lowest loading rate because there exists the widest local region with high matrix crack density at 0.019 kN/s, as shown in Fig. 10.

As for the peaks of local strain at each labelled concentration region, their numbers and locations are related to both the occurring sequences and positions of transverse matrix cracks. Both single peak and multiple peaks of local strain profiles exist in the labelled strain concentration regions during the tests, as Fig. 11 presents. In the single-peak case, the location of the peak strain almost stays at the initial place (as shown from t_1 to t_2 in Fig. 11(a)-(c), (e)) if the updated minimum crack spacing is always located around the first crack generated at the labelled concentration region. Otherwise, it shifts to the position near the newest crack (as shown from t_1 to t_2 in Fig. 11(d)), or turns to multi-peak cases (as shown from t_2 to t_3 in Fig. 11). In the multi-peak cases, valleys usually exist among neighbor peaks at each strain concentration region and the strain differences of each pair of valley and peak are determined by the related crack spacing. The larger the crack spacing is, higher strain differences occur. Furthermore, similar to the location of the single-peak case, the highest peak in the multi-peak region is positioned at either the location of the newest crack or near the place with the minimum crack spacing.

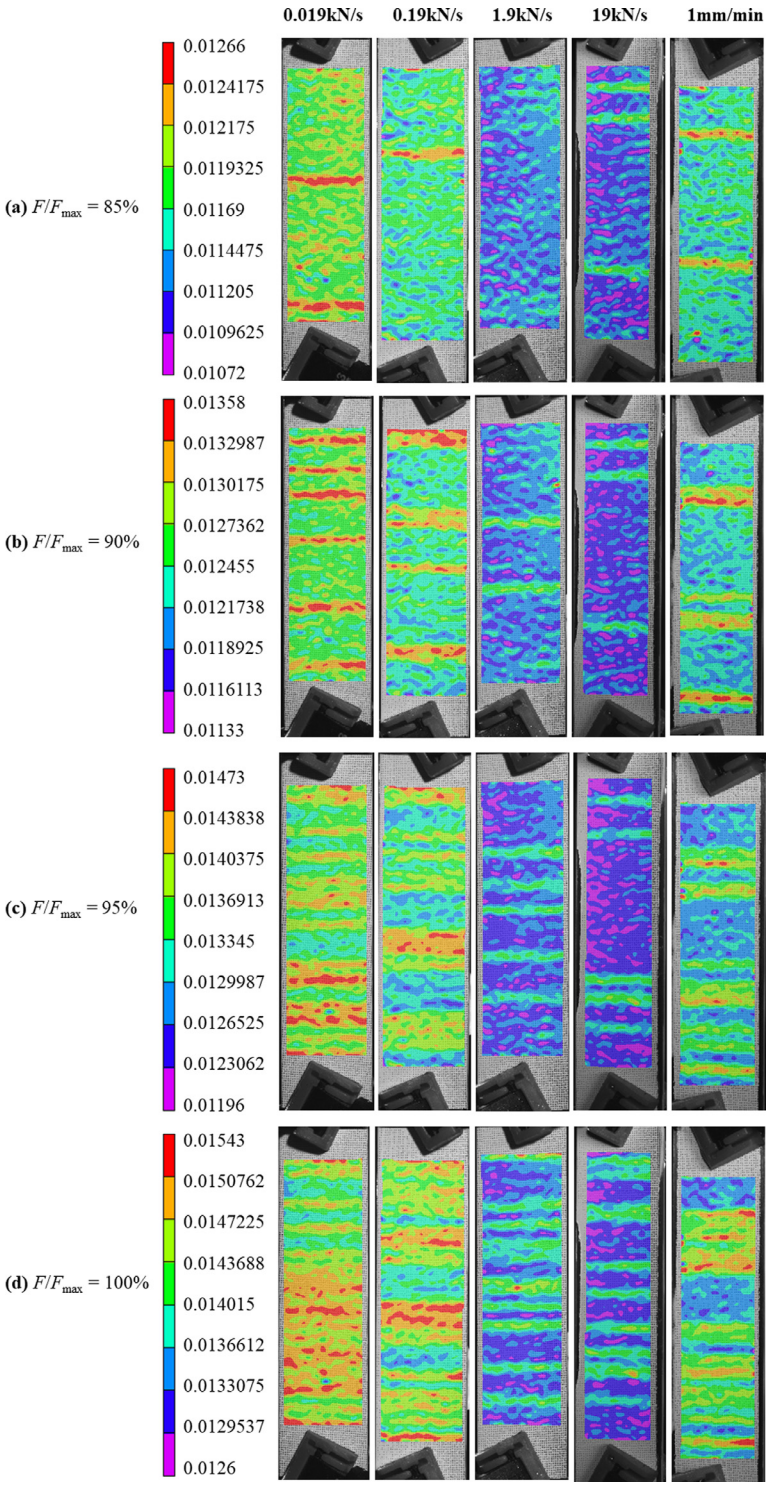

Fig. 9. Axial strain distributions at the outer 0° ply under four different load levels for each loading rates.

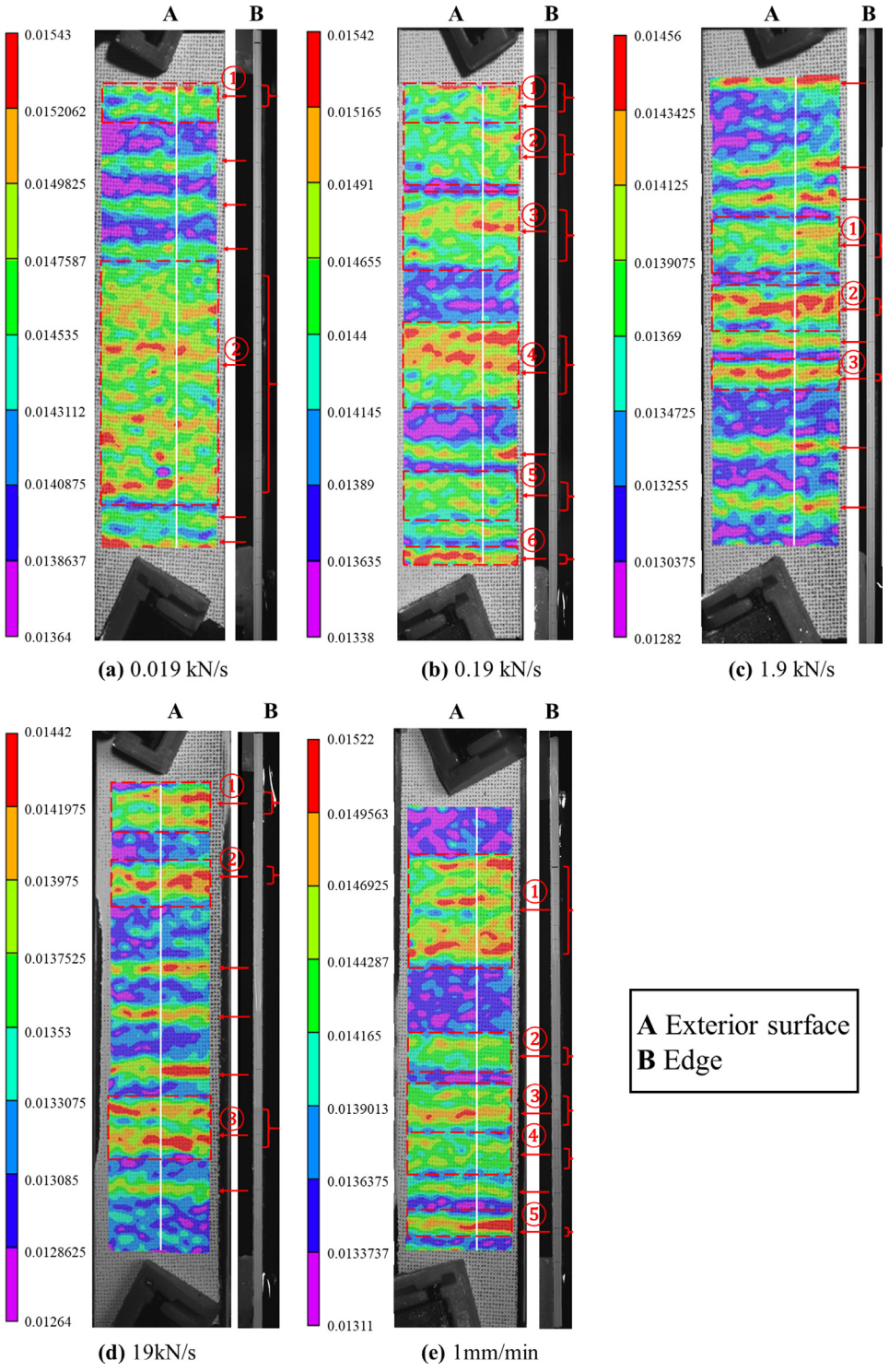

Fig. 10. Correlation between strain concentrations at the exterior 0° ply and transverse matrix cracks generated from the edge thickness at the maximum load under different loading rates.

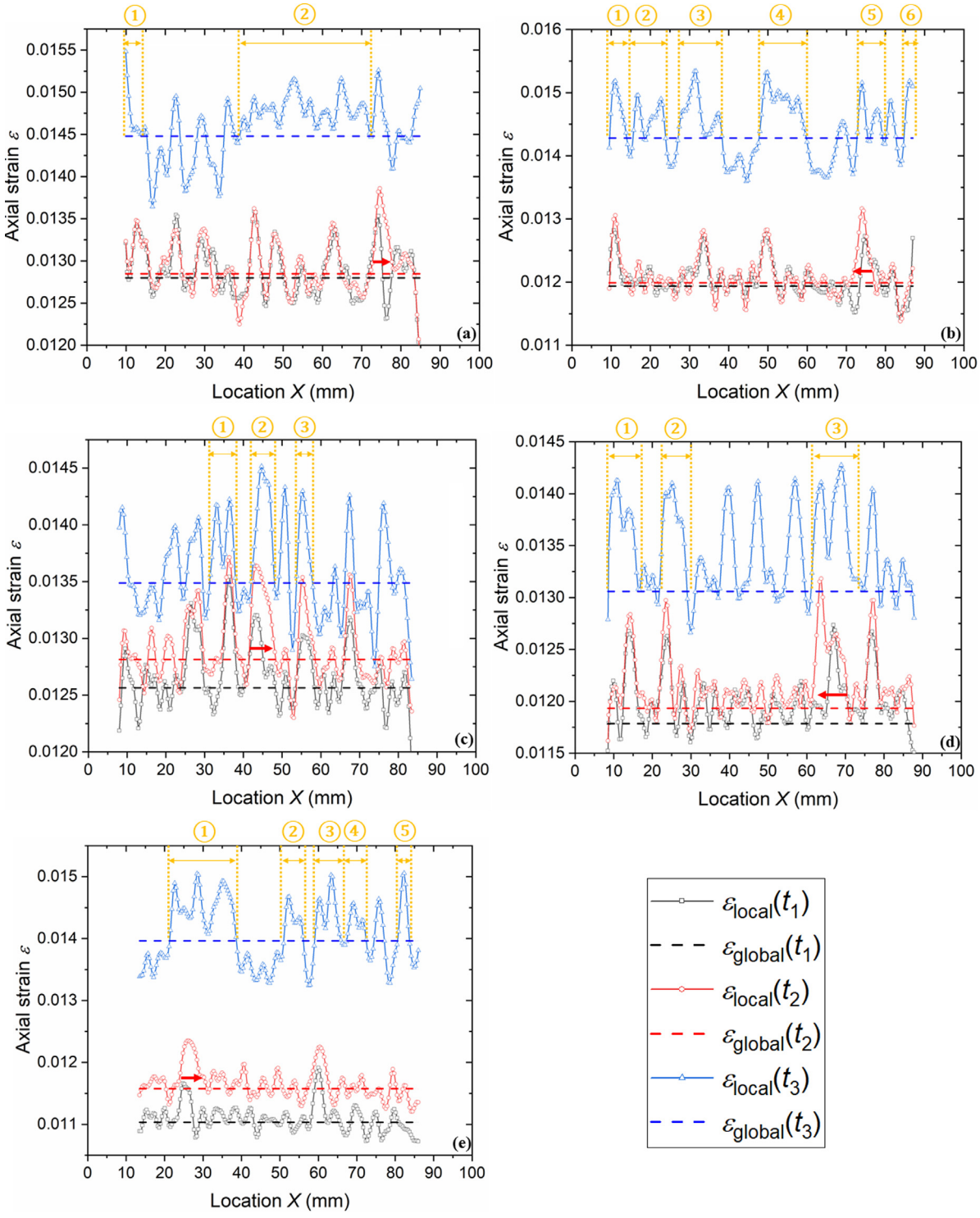

Fig. 11. Strain profile of a line slice along the loading direction at three different moments:(a) 0.019 kN/s, (b) 0.19 kN/s, (c) 1.9 kN/s, (d) 19 kN/s, (e) 1 mm/min.

4. Conclusion

This paper investigated the loading rate effects on the mechanical properties and the damage accumulation process of $[0^{\circ}_2/90^{\circ}_4]_S$ carbon fiber-polymer laminates under tensile loading. Emphasis was given on characterizing the distribution of transverse matrix cracks and how the occurrence of inter-laminar cracks could influence the transverse matrix density. Three in-situ monitoring techniques, edge-camera, DIC and AE were employed to monitor simultaneously and synergistically the damage accumulation process. The main conclusions are listed hereafter:

1) The axial modulus and strength are less sensitive to different loading rates than the failure strain, which decreases with the increase of the loading rate.
2) At low loading rate, the maximum density of transverse matrix cracks is high, and inter-laminar cracks at the $0^{\circ}/90^{\circ}$ interfaces are more likely to initiate from tips of the transverse matrix cracks. The

local damage pattern has a H-shape where transverse matrix and inter-laminar cracks coexist. When the loading rate is lower than 0.19 kN/s, the density of transverse matrix cracks slightly decreases due to the constrains imposed by the inter-laminar cracks.

3) Transverse matrix cracks distributed more uniformly under lower loading rates, accompanied with smaller scatter of crack spacing at local regions, while a more random distribution pattern is found under higher loading rates.
4) The cumulative energy of AE activity in the range of 100–200 kHz was linearly correlated to the density of transverse matrix cracks. This observation paves a promising way for the real-time quantification of crack evolution based solely on the AE activity.
5) Narrow strips of strain concentration occurred at the exterior 0° ply once transvers matrix cracks initiated and a correlation between the number of strips and the number of cracks was found. The strips, at a later stage, expanded or connected with one another to form wide concentration regions. The largest strain concentration region was presented at the lowest rate (0.019 kN/s) where local crack density is high enough to induce the expansions and connections of narrow strips of strain concentration.
6) Spatial consistence was observed between transverse matrix cracks at edges and stress concentrations at the exterior 0° ply from DIC. The peaks of axial strain were located either near the newest developed cracks or at the place with the minimum crack spacing.

Declaration of Competing Interest

The authors declare that they have no known competing financial interests or personal relationships that could have appeared to influence the work reported in this paper.

Acknowledgments

The authors would like to thank the financial supports of China Scholarship Council (No.201706290028).

References

[1] N. Taniguchi, T. Nishiwaki, H. Kawada, Tensile strength of unidirectional CFRP laminate under high strain rate, Adv. Compos. Mater. Off. J. Jpn. Soc. Compos. Mater. 16 (2007) 167–180, doi:10.1163/156855107780918937.
[2] A. Gilat, R.K. Goldberg, G.D. Roberts, Experimental study of strain-rate-dependent behavior of carbon/epoxy composite, Compos. Sci. Technol. 62 (2002) 1469–1476, doi:10.1016/S0266-3538(02)00100-8.
[3] X. Zhang, Y. Shi, Z.X. Li, Experimental study on the tensile behavior of unidirectional and plain weave CFRP laminates under different strain rates, Compos. Part B Eng. 164 (2019) 524–536, doi:10.1016/j.compositesb.2019.01.067.
[4] K. Naresh, K. Shankar, B.S. Rao, R. Velmurugan, Effect of high strain rate on glass/carbon/hybrid fiber reinforced epoxy laminated composites, Compos. Part B Eng. 100 (2016) 125–135, doi:10.1016/j.compositesb.2016.06.007.
[5] D. Ma, A. Manes, S.C. Amico, M. Giglio, Ballistic strain-rate-dependent material modelling of glass-fibre woven composite based on the prediction of a meso-heterogeneous approach, Compos. Struct. 216 (2019) 187–200, doi:10.1016/j.compstruct.2019.02.102.
[6] J. Raghavan, M. Meshii, Time-dependent damage in carbon reinforced polymer composites *, Compos. Part A 27 (1996) 1223–1227, doi:10.1016/1359-835X(96)00073-5.
[7] T.H. Nguyen, D. Gamby, Effects of nonlinear viscoelastic behaviour and loading rate on transverse cracking in CFRP laminates, Compos. Sci. Technol. 67 (2007) 438–452, doi:10.1016/j.compscitech.2006.08.027.
[8] J. Berthe, M. Ragonet, Passive infrared thermography measurement of transverse cracking evolution in cross-ply laminates. Strain 2018:1–15. doi:10.1111/str.12293.
[9] M. Azadi, H. Sayar, A. Ghasemi-Ghalebahman, S.M. Jafari, Tensile loading rate effect on mechanical properties and failure mechanisms in open-hole carbon fiber reinforced polymer composites by acoustic emission approach, Compos. Part B Eng. 158 (2019) 448–458, doi:10.1016/j.compositesb.2018.09.103.
[10] M. Mehdikhani, E. Steensels, A. Standaert, K.A.M. Vallons, L. Gorbatikh, S.V. Lomov, Multi-scale digital image correlation for detection and quantification of matrix cracks in carbon fiber composite laminates in the absence and presence of voids controlled by the cure cycle, Compos. Part B Eng. 154 (2018) 138–147, doi:10.1016/j.compositesb.2018.07.006.
[11] F.E. Oz, N. Ersoy, M. Mehdikhani, S.V. Lomov, Multi-instrument in-situ damage monitoring in quasi-isotropic CFRP laminates under tension, Compos. Struct. 196 (2018) 163–180, doi:10.1016/j.compstruct.2018.05.006.
[12] F.E. Oz, N. Ersoy, S.V. Lomov, Do high frequency acoustic emission events always represent fibre failure in CFRP laminates? Compos. Part A Appl. Sci. Manuf. 103 (2017) 230–235, doi:10.1016/j.compositesa.2017.10.013.
[13] C. Baker, G.N. Morscher, V.V. Pujar, J.R. Lemanski, Transverse cracking in carbon fiber reinforced polymer composites: modal acoustic emission and peak frequency analysis, Compos. Sci. Technol. 116 (2015) 26–32, doi:10.1016/j.compscitech.2015.05.005.
[14] L. Zubillaga, A. Turon, J. Renart, J. Costa, P. Linde, An experimental study on matrix crack induced delamination in composite laminates, Compos. Struct. 127 (2015) 10–17, doi:10.1016/j.compstruct.2015.02.077.
[15] Cho C., Holmes J.W., Barber J.R., Arbor A. Distribution of matrix cracks in a uniaxial ceramic composite. J. Am. Ceram. Soc. 1992:316–24. doi:10.1111/j.1151-2916.1992.tb08181.x.
[16] A. Tessema, S. Ravindran, A. Kidane, Gradual damage evolution and propagation in quasi-isotropic CFRC under quasi-static loading, Compos. Struct. 185 (2018) 186–192, doi:10.1016/j.compstruct.2017.11.013.
[17] Z. Zhao, P. Liu, C. Chen, C. Zhang, Y. Li, Modeling the transverse tensile and compressive failure behavior of triaxially braided composites, Compos. Sci. Technol. 172 (2019) 96–107, doi:10.1016/j.compscitech.2019.01.008.
[18] J. Huang, M.L. Pastor, C. Garnier, X.J. Gong, A new model for fatigue life prediction based on infrared thermography and degradation process for CFRP composite laminates, Int. J. Fatigue 120 (2019) 87–95, doi:10.1016/j.ijfatigue.2018.11.002.
[19] V. Munoz, B. Valès, M. Perrin, M.L. Pastor, H. Welemane, A. Cantarel, et al., Damage detection in CFRP by coupling acoustic emission and infrared thermography, Compos. Part B Eng. 85 (2016) 68–75, doi:10.1016/j.compositesb.2015.09.011.
[20] M. Saeedifar, M.A. Najafabadi, D. Zarouchas, H.H. Toudeshky, M. Jalalvand, Clustering of interlaminar and intralaminar damages in laminated composites under indentation loading using acoustic emission, Compos. Part B Eng. 144 (2018) 206–219, doi:10.1016/j.compositesb.2018.02.028.
[21] M.G.R. Sause, S. Schmitt, S. Kalafat, Failure load prediction for fiber-reinforced composites based on acoustic emission, Compos. Sci. Technol. 164 (2018) 24–33, doi:10.1016/j.compscitech.2018.04.033.
[22] C. Huang, S. Ju, M. He, Q. Zheng, Y. He, J. Xiao, et al., Identification of failure modes of composite thin-ply laminates containing circular hole under tension by acoustic emission signals, Compos. Struct. 206 (2018) 70–79, doi:10.1016/j.compstruct.2018.08.019.
[23] R. Mohammadi, M.A. Najafabadi, M. Saeedifar, J. Yousefi, G. Minak, Correlation of acoustic emission with finite element predicted damages in open-hole tensile laminated composites, Compos. Part B Eng. 108 (2016) 427–435, doi:10.1016/j.compositesb.2016.09.101.
[24] V. Arumugam, K. Saravanakumar, C. Santulli, Damage characterization of stiffened glass-epoxy laminates under tensile loading with acoustic emission monitoring, Compos. Part B Eng. 147 (2018) 22–32, doi:10.1016/j.compositesb.2018.04.031.
[25] M. Saeedifar, D. Zarouchas, Damage characterization of laminated composites using acoustic emission: a review, Compos. Part B Eng. 175 (2020) 108039, doi:10.1016/j.compositesb.2020.108039.
[26] J. Kupski, S. Teixeira de Freitas, D. Zarouchas, P.P. Camanho, R. Benedictus, Composite layup effect on the failure mechanism of single lap bonded joints, Compos. Struct. 217 (2019) 14–26, doi:10.1016/j.compstruct.2019.02.093.
[27] Hexcel. HexPly ® 6376 - Product Data Sheet - EU Version 2016:1–2.
[28] ASTM-American Society for Testing and Materials. ASTM D3039/D3039M: standard Test Method for Tensile Properties of Polymer Matrix Composite Materials. Annu. B ASTM Stand.2014:1–13. doi:10.1520/D3039.
[29] R.O. Ochola, K. Marcus, G.N. Nurick, T. Franz, Mechanical behaviour of glass and carbon fibre reinforced composites at varying strain rates, Compos. Struct. 63 (2004) 455–467, doi:10.1016/S0263-8223(03)00194-6.
[30] Y. Zhang, P.-.Y. Ben Jar, S. Xue, L. Li, L. Han, Damage evolution in high density polyethylene under tensile, compressive, creep and fatigue loading conditions, Eng. Fract. Mech. (2019), doi:10.1016/j.engfracmech.2019.05.008.
[31] A. Gilat, R.K. Goldberg, G.D. Roberts, Strain rate sensitivity of epoxy resin in tensile and shear loading, J. Aerosp. Eng. 20 (2007) 75–89 doi:10.1061/(asce)0893-1321(2007)20:2(75).
[32] Y. Zhou, Y. Wang, Y. Xia, S. Jeelani, Tensile behavior of carbon fiber bundles at different strain rates, Mater. Lett. 64 (2010) 246–248, doi:10.1016/j.matlet.2009.10.045.
[33] J.-.M. Berthelot, P. Leblond, A. El Mahi, J.-.F. Le Corre, Transverse cracking of cross-ply laminates: part 1. Analysis, Compos. Part A Appl. Sci. Manuf. 27 (1996) 989–1001, doi:10.1016/1359-835X(96)80002-A.
[34] V.V. Silberschmidt, Matrix cracking in cross-ply laminates: effect of randomness, Compos. Part A Appl. Sci. Manuf. 36 (2005) 129–135, doi:10.1016/j.compositesa.2004.06.008.
[35] P. Maimí, P.P. Camanho, J.A. Mayugo, A. Turon, Mechanics of Materials Matrix cracking and delamination in laminated composites. Part II : evolution of crack density and delamination, Mech. Mater. 43 (2011) 194–211, doi:10.1016/j.mechmat.2011.01.002.
[36] V. Vinogradov, Z. Hashin, Probabilistic energy based model for prediction of transverse cracking in cross-ply laminates, Int. J. Solids Struct. 42 (2005) 365–392, doi:10.1016/j.ijsolstr.2004.06.043.
[37] Groves S.E., Harris C.E., Highsmith A.L., Allen D.H., Norvell R.G. An experimental and analytical treatment of matrix cracking in cross-ply laminates. Exp. Mech. 1987:73–9.

[38] S. Hu, J.S. Bark, J.A. Nairn, On the phenomenon of curved microcracks in [(S)/90n] s laminates: their shapes, initiation angles and locations, Compos. Sci. Technol. 47 (1993) 321–329, doi:10.1016/0266-3538(93)90001-W.

[39] C.V. Singh, R. Talreja, Evolution of ply cracks in multidirectional composite laminates, Int. J. Solids Struct. 47 (2010) 1338–1349, doi:10.1016/j.ijsolstr.2010.01.016.

[40] N.A. Petrov, L. Gorbatikh, S.V. Lomov, A parametric study assessing performance of eXtended Finite Element Method in application to the cracking process in cross-ply composite laminates, Compos. Struct. 187 (2018) 489–497, doi:10.1016/j.compstruct.2017.12.014.

[41] Q.Q. Ni, M. Iwamoto, Wavelet transform of acoustic emission signals in failure of model composites, Eng. Fract. Mech. 69 (2002) 717–728, doi:10.1016/S0013-7944(01)00105-9.

[42] Vallen Systeme GmbH. Verification of the AE signal processor, parametric input channels and system performance according to EN 13477-2:2010 2019:26.